A Lagrangian Study of Precipitation-Driven Downdrafts*

GIUSEPPE TORRI

Department of Earth and Planetary Sciences, Harvard University, Cambridge, Massachusetts

ZHIMING KUANG

Department of Earth and Planetary Sciences, and School of Engineering and Applied Sciences, Harvard University, Cambridge, Massachusetts

(Manuscript received 29 July 2015, in final form 9 November 2015)

ABSTRACT

Precipitation-driven downdrafts are an important component of deep convective systems. They stabilize the atmosphere by injecting relatively cold and dry air into the boundary layer. They have also been invoked as responsible for balancing surface latent and sensible heat fluxes in the heat and moisture budget of tropical boundary layers. This study is focused on precipitation-driven downdrafts and basic aspects of their dynamics in a case of radiative–convective equilibrium. Using Lagrangian particle tracking, it is shown that such downdrafts have very low initial heights, with most parcels originating within 1.5 km from the surface. The tracking is also used to compute the contribution of downdrafts to the flux of moist static energy at the top of the boundary layer, and it is found that this is on the same order of magnitude as the contribution due to convective updrafts, but much smaller than that due to turbulent mixing across the boundary layer top in the environment. Furthermore, considering the mechanisms driving the downdrafts, it is shown that the work done by rain evaporation is less than half that done by condensate loading.

1. Introduction

The existence of downdrafts in deep convective systems was acknowledged as early as a hundred years ago by Humphreys (1914), who also hypothesized that they are maintained by the evaporation of rain falling through unsaturated air. Since then, downdrafts have been the focus of many studies (e.g., Knupp and Cotton 1985; Cotton et al. 2011, and references therein), which have led to a considerable advancement of our understanding of these phenomena and, more generally, of precipitating convection.

Within the category of downdrafts, we would like to concentrate on *precipitation-driven downdrafts*, by which, following the nomenclature explained in Knupp and Cotton (1985), we mean those downdrafts that appear in the presence of precipitation and that reach the surface, injecting masses of cold and dry air in the subcloud layer (e.g., Byers and Braham 1949; Fankhauser 1976; Barnes and Garstang 1982; Knupp 1987, 1988).

From a rather practical point of view, precipitation-driven downdrafts have been of interest for some time, given their potential to generate *downbursts* and *microbursts*, very strong currents of air with vertical velocities often exceeding $10\,\mathrm{m\,s^{-1}}$ in magnitude (see, e.g., Fujita 1985, 1986; Proctor 1988, 1989; Wakimoto et al. 1994). These intense downdrafts can be found in cases where precipitating clouds are formed above deep and dry boundary layers—such as over the Great Plains—and constitute a serious hazard for civil aviation.

From a more conceptual perspective, throughout the years precipitation-driven downdrafts have been studied in different contexts, an important example being that of the so-called boundary layer quasi-equilibrium (BLQE) hypothesis (Emanuel 1989; Raymond 1994, 1995), proposed to explain why the moist entropy of tropical boundary layers seems to change very little with time. Simply put, according to this hypothesis, the moistening and heating of the tropical boundary layer provided by

* Supplemental information related to this paper is available at the Journals Online website: http://dx.doi.org/10.1175/JAS-D-15-0222.s1.

Corresponding author address: Giuseppe Torri, Department of Earth and Planetary Sciences, Harvard University, 20 Oxford Street, Cambridge, MA 02138.
E-mail: torri@fas.harvard.edu

DOI: 10.1175/JAS-D-15-0222.1

the surface fluxes are counterbalanced mainly by precipitation-driven downdrafts that bring low-entropy air from the midtroposphere to the surface. As argued by Raymond (1995), the turbulent entrainment at the top of the boundary layer plays little role in the balance. This explanation is in contrast with the hypothesis used by Arakawa and Schubert (1974) in their cumulus parameterization, where it is mixing with the environmental air and, sometimes, horizontal advection, which balance the action of surface fluxes. These two hypotheses were recently examined and tested by Thayer-Calder and Randall (2015) with a numerical model. Interestingly, their results suggest that only a small fraction of the flux of moist static energy (MSE) at the top of the boundary layer is due to precipitation-driven downdrafts.

Another framework in which precipitation-driven downdrafts are of considerable importance is that of convection triggering. The masses of air injected by downdrafts in the subcloud layer spread horizontally on the surface as density currents, usually called *cold pools*, which are one of the main factors responsible for maintaining deep convective systems (Purdom 1976; Weaver and Nelson 1982). In organized cases, such as squall lines or supercell thunderstorms, it has been known for a long time (see, e.g., Rotunno and Klemp 1985; Rotunno et al. 1988; Weisman et al. 1988; Weisman and Rotunno 2004) that the interaction between the gust front of cold pools and the wind shear or the collision between two or more cold pools can provide enough kinetic energy to parcels at the surface to reach their level of free convection (LFC). In nonorganized cases, parcels reach their LFC through a cooperation of the gust-front lifting and the thermodynamic effect provided by the positive moisture anomaly at the leading edge of cold pools, which reduces the convective inhibition experienced by parcels above the lifting condensation level (Tompkins 2001; Torri et al. 2015). The influence of precipitation-driven downdrafts on convection triggering is indirect but, nevertheless, strong: by controlling the initial conditions of cold pools, downdrafts effectively control the strength of the cold pools' gust fronts and their ability to lift parcels from the surface and, potentially, also the magnitude of the thermodynamic effect.

In this study, we will consider a tropical maritime environment, and we will focus on three fundamental aspects of precipitation-driven downdraft dynamics:

1) What is the initial height of a precipitation-driven downdraft?
2) What is the contribution of precipitation-driven downdrafts to the budget of MSE in the subcloud layer?
3) What is the role of condensate loading versus rain evaporation in maintaining a precipitation-driven downdraft?

To some extent, these topics have been addressed in the past in various studies, although using limited techniques that did not provide an entirely clear answer. For instance, starting from as early as Mal and Desai (1938), the typical approach to diagnose the initial height of downdrafts, sometimes referred to as *source level*, has been to use thermodynamic properties of downdraft air, like the wet-bulb potential temperature θ_w, the equivalent potential temperature θ_e, or MSE, which are approximately conserved in adiabatic processes and water vapor–liquid water phase transitions (see also, e.g., Mal and Desai 1938; Normand 1946; Newton 1950; Zipser 1969; Betts 1976; Fankhauser 1976; Lemon 1976; Barnes and Garstang 1982; Johnson and Nicholls 1983; Kingsmill and Houze 1999). The problem with this approach is that it assumes that mixing is negligible and that all the downdraft air originates at the initial height, neither of which hypotheses are necessarily true.

Analogously, various authors have asked what mechanisms maintain precipitation-driven downdrafts, recognizing rain evaporation and condensate loading as leading factors (Byers and Braham 1949; Braham 1952; Fankhauser 1976; Lemon 1976; Barnes and Garstang 1982; Knupp and Cotton 1985). However, the extent to which one mechanism is dominant over the other even in simple cases of unorganized convection remains unclear.

In this manuscript, we will address the two questions outlined above mainly using a Lagrangian particle dispersion model (LPDM). Compared to the techniques that have been used in the past, the LPDM provides a great deal of information. In particular, analyzing the position of millions of particles released in the simulation domain will allow us to determine the initial height of a downdraft in a clear and simple manner. Also, combining the output from the LES model that we will use with the Lagrangian history of the particles from when they enter a precipitation-driven downdraft until their exit near the surface, we will be able to quantify the importance of rain evaporation and condensate loading in driving the downdraft.

Notice that the use of particles' trajectories to study downdrafts is a path that has been explored in the past: Miller and Betts (1977), for example, used them to illustrate the behavior of downdrafts in Venezuelan convective storms, and Knupp (1988) used them in the context of storms in the high plains. However, the computational limitations of the past did not allow for the simulation of a number of trajectories large enough to make significant statistics.

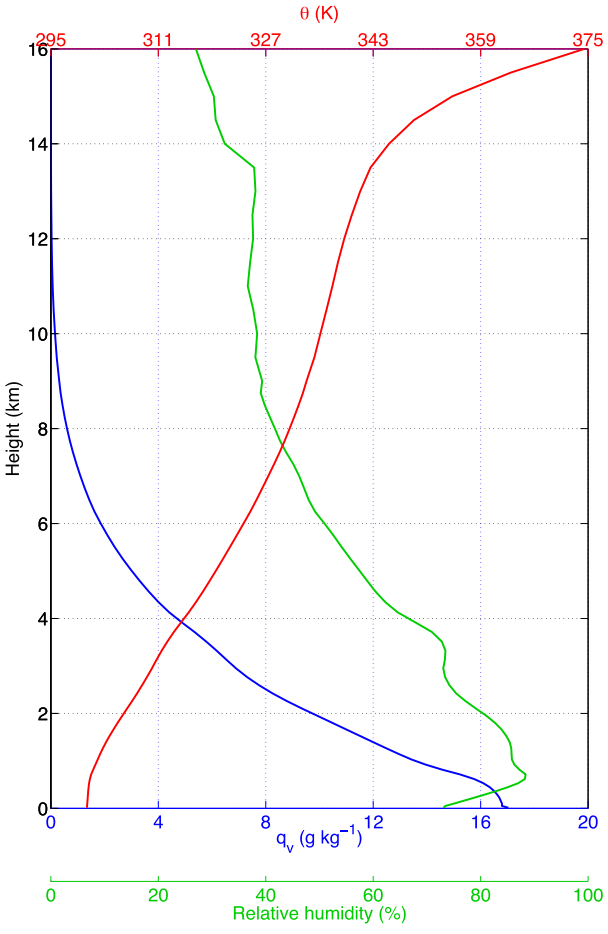

FIG. 1. Time average of the vertical profiles of potential temperature (red), water vapor specific humidity (blue), and relative humidity (green).

2. Methods

The model used in this study is the System for Atmospheric Modeling (SAM), version 6.8.2, which solves the anelastic equations of motion and uses liquid water static energy and nonprecipitating and precipitating total water as thermodynamic prognostic variables (Khairoutdinov and Randall 2003). The equations are solved with doubly periodic boundary conditions in the horizontal directions. A prognostic turbulent kinetic energy 1.5-order closure scheme is used to parameterize subgrid-scale effects.

We ran the model with the Lin microphysics scheme, a single-moment scheme that predicts the specific humidities of water vapor, cloud liquid water, cloud ice, rain, snow, and graupel (Lin et al. 1983). The surface fluxes are computed using the Monin–Obukhov similarity theory.

The simulations are carried out over a domain of $64 \times 64\,\mathrm{km}^2$ in the horizontal directions and 30 km in the vertical. The grid size in the horizontal directions is 250 m, and it varies in the vertical: 500 m above 10 km, which decrease progressively to 38 m close to the model surface. The time step is 3 s. Figure 1 shows the environment vertical profiles of potential temperature (red), water vapor specific humidity (blue), and relative humidity (green), averaged over the duration of the simulation.

We ran the model with the LPDM discussed in Nie and Kuang (2012). For every column in the domain, the LPDM is initialized with 1120 particles, their positions being distributed randomly over the bottom 18 km of the model domain, with a probability distribution that is a uniform function of pressure. A validation of the LPDM can be found in the supplemental information.

Every minute of simulated time, the positions of the Lagrangian particles and the three-dimensional model fields from SAM are recorded. A cross-comparison of Lagrangian and Eulerian data provides the complete histories of thermodynamic and dynamic properties of the particles.

Throughout the simulation, the sea surface temperature is held constant at 302.65 K, and the diurnal cycle is removed by fixing the zenith angle at 51.7° with solar constant halved to $685\,\mathrm{W\,m^{-2}}$. The mean winds are initialized to zero. We first ran the model for 30 days without Lagrangian particles on the same domain until radiative–convective equilibrium (RCE) is reached. At the end of this period, we restarted the simulation with the Lagrangian particles and collected data for 12 h of model time. No nudging was imposed on the horizontal winds. The precipitation rate averaged in time during the 12 h of data collection and in space over the entire domain is $3.4\,\mathrm{mm\,day^{-1}}$.

We define the *subcloud layer* as the portion of the model domain that includes the surface and in which the time- and domain-averaged cloud liquid water specific humidity q_l is below $10^{-5}\,\mathrm{g\,kg^{-1}}$. With the chosen settings, this corresponds to the bottom 531 m of the domain.

We define the density potential temperature of a particle as follows (Emanuel 1994):

$$\theta_\rho = \theta\left[1 + \left(\frac{R_v}{R_d} - 1\right)q_v - q_l\right], \tag{1}$$

where R_d and R_v are the gas constants of dry air and water vapor and equal 287 and $461\,\mathrm{J\,kg^{-1}\,K^{-1}}$, respectively, and q_v is the specific humidity of water vapor. As customary, we define $\varepsilon = (R_v/R_d - 1)$ and will use this convention for the remainder of this manuscript.

We say that a grid box in the subcloud layer is part of the core of a cold pool if its density potential

temperature θ_ρ is lower than the horizontal average by 1.5 K.[1] This definition was chosen after examining the model outputs and only serves to separate the part of the cold pool that is fed by the precipitation-driven downdraft from the rest (cf. Torri et al. 2015). As shown in the supplemental information, the analysis presented in the following section is not particularly sensitive to the value chosen for the threshold.

We consider as part of a precipitation-driven downdraft all particles from any altitude that acquire and maintain negative vertical velocity until they enter the core of a cold pool. Interestingly, although we do not require the precipitation-driven downdraft to be unsaturated, most of the descent of the particles in precipitation-driven downdrafts takes place in unsaturated grid boxes.

3. Results

Having laid out the research questions in section 1, and after having explained how we pursue these questions in the section 2, we will now discuss our findings.

a. *On the initial height of precipitation-driven downdrafts*

Following the definition of precipitation-driven downdraft that we have given in the previous section, whenever a particle enters the core of a cold pool, we track its position back in time for every step during which the particle was in grid boxes that satisfied the condition that the vertical wind $w \leq 0\,\mathrm{m\,s^{-1}}$. The height of the first grid box for which the previous condition is true is taken as the initial height of the particle we sampled.

Notice that, because the coldest regions of cold pools are known to exhibit high pressure perturbations, the model outputs show that the vertical velocity of precipitation-driven downdrafts as they approach the surface decreases considerably (cf. Fig. 10 later in the text). When the vertical velocity is small enough, turbulent or wave fluctuations may cause its values in some grid boxes to oscillate between positive and negative. There follows that, if we were to apply the definition of precipitation-driven downdraft given above, a considerable number of sampled particles would appear to have originated close to the surface. To avoid this problem, whenever the vertical velocity of a particle in a downdraft turns positive, a clock is started as the particles' positions are scanned backward in time; if the vertical velocity becomes negative again within 10 min from the start of the clock, the particle is still considered part of the downdraft; otherwise, it is dismissed. Sensitivity tests presented in the supplemental information show that the results and our conclusions are not particularly sensitive to the precise value chosen for the time threshold. Furthermore, in order to avoid interference from fast detrainment–entrainment events in cold pools, once a particle ends up in a cold pool core and its properties are recorded, the particle is flagged and discarded for the rest of the simulation.

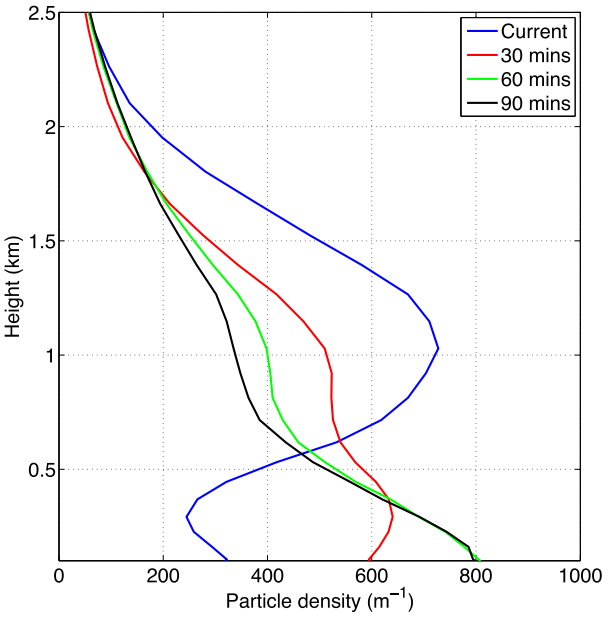

FIG. 2. Distribution of Lagrangian particles' positions at various times before becoming part of a precipitation-driven downdraft. The red, green, and black curves refer to positions 30, 60, and 90 min before entering the downdraft, respectively. The blue curve shows the distribution of positions at the time of entrance.

In Fig. 2, the blue curve shows the distribution of initial heights of all particles that were injected in the core of a cold pool by a precipitation-driven downdraft. Notice that the distribution is confined almost entirely to the bottom of the troposphere: 98% of particles have initial heights lower than 2.5 km. The curve shows a pronounced peak at approximately 1 km of altitude, just a few hundred meters above the top of the subcloud layer, and a smaller one near the surface. Examination of trajectories for particles that contribute to the lower peak shows that most of these particles descended from higher altitudes with a precipitation-driven downdraft, but, near the surface, their vertical velocity, however small, was positive for more than 10 min before they entered the core of a cold pool.

These results are nicely in accordance with existing literature, which suggested that, for tropical convection, the source level of precipitation-driven downdrafts is just

[1] For brevity, whenever a particle enters a grid box that is part of the core of a cold pool, we will simply say that "the particle enters/belongs to the core of a cold pool."

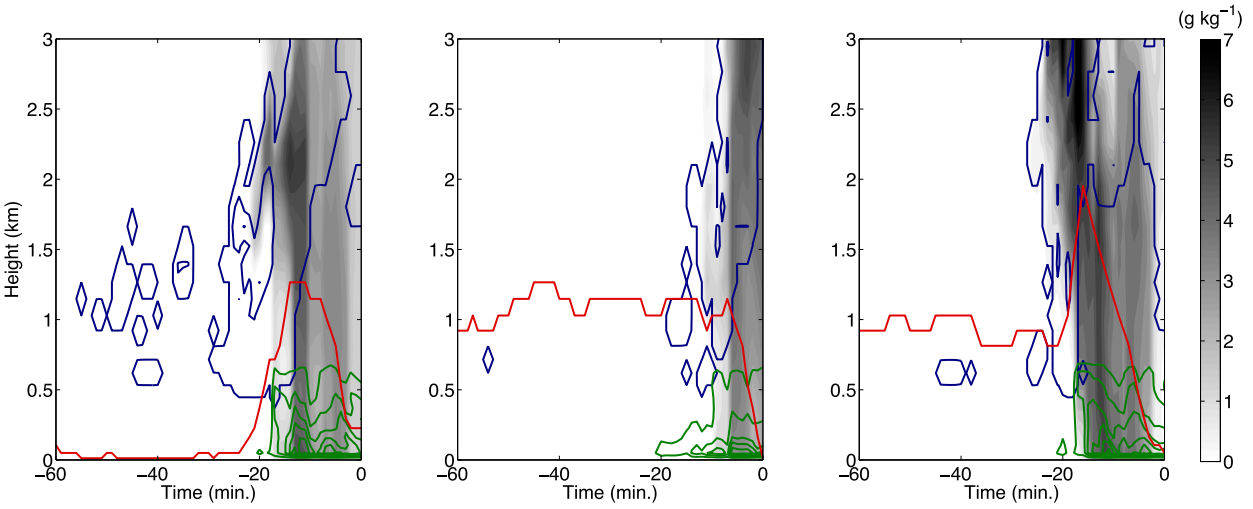

FIG. 3. Three examples of Lagrangian particles' histories 60 min before entering the core of a cold pool are shown with a red line. (left) An up–down downdraft, (middle) a midlevel downdraft originating at ~1 km, and (right) a hybrid between the two. The blue contours represent the specific humidity of total nonprecipitating water at increasing intervals of 1 g kg^{-1}. The green contours show negative buoyancy in the subcloud layer at decreasing intervals of 0.02 m s^{-2} starting at −0.01 m s^{-2}. The gray shading represents the specific humidity of total precipitating water. The values shown for all variables at different heights refer to the vertical column where the particle is.

above cloud base [see, e.g., Zipser (1969), Betts (1976), and Kingsmill and Houze (1999), just to cite a few].

We should point out that the initial height of a downdraft may still carry along some ambiguity. For example, it could be that a number of particles that entered the precipitation-driven downdraft at 1 km actually originated from much greater altitudes: they were transported down by another downdraft from which they eventually left, and then, after some time, they became part of the precipitation-driven downdraft that carried them down to the surface. A simple way to check whether this is the case is to ask where the particles were before entering the precipitation-driven downdraft.

The red, green, and black curves in Fig. 2 show the distribution of the sampled particles' positions 30, 60, and 90 min before entering the precipitation-driven downdraft, respectively. They can be thought of as the evolution back in time of the blue curve. Interestingly, the red curve suggests that 61% of particles actually come from the subcloud layer, whereas the remaining seem to originate near the height where they entered the downdraft. According to the nomenclature discussed in Knupp (1988), we will refer to the former as *up–down* and to the latter as *midlevel*. Less than 2% of all particles originate from an altitude greater than 2.5 km.

To better appreciate the history of the Lagrangian particles prior to their entrance in a precipitation-driven downdraft, we can look directly at the trajectories of a few representative cases. The red lines in Fig. 3 show the time evolution of the vertical positions of three particles for the 60 min before they enter the core of a cold pool. Notice that the horizontal axis represents the time in the particles' histories, with 0 min being the moment they enter a cold pool's core. The particles have been selected rather arbitrarily, but an extensive scan through a large number of particles' histories makes us confident the particular examples shown illustrate well the possible scenarios for downdrafts.

In all panels, the blue contours represent the total nonprecipitating water specific humidity q_n, whereas the green contours represent the buoyancy. To keep the image clean, we only show contours for negative buoyancy and only for the subcloud layer. Finally, the gray shading represents the total precipitating water specific humidity q_p.

Figure 3 (left) shows the history of a particle in an up–down downdraft. As can be seen, the particle is lifted from the surface at approximately −25 min by the gust front of an expanding cold pool, indicated by the appearance of the negative buoyancy contours in the subcloud layer, and it quickly becomes part of an updraft. As the particle ascends, it reaches lifting condensation level (LCL), and soon afterward it enters a precipitating column. The precipitation experienced by the particle is sufficient to change the sign of its buoyancy and stop its ascension. As a result, the particle leaves the updraft and enters a downdraft that becomes unsaturated almost immediately. The descent continues with no interruptions until the particle reaches the core of a cold pool. Curiously, visual inspection of the three-dimensional model output suggests that the particle enters the same cold pool that had lifted it from the surface.

Figure 3 (middle) shows the history of a particle that descends to the surface levels through a midlevel downdraft. As might be expected, the particle sits in an almost undisturbed environment for most of its life. The changes in altitude in clear sky seem to be due to random turbulent fluctuations or gravity waves. Then, at approximately −20 min, the particle is entrained into a cloud, where its buoyancy becomes negative. The particle starts descending and enters the core of a cold pool at the surface.

Finally, Fig. 3 (right) shows another possible scenario for particles entering precipitation-driven downdrafts—one that, to some extent, is a mixture of the previous two. The particle represented in the figure starts off at an altitude of approximately 1 km, subject only to random turbulence or wave motions, which cause its position to oscillate a little. At −20 min, the particle becomes part of an updraft that makes it rise to an altitude of 2 km, where, finally, its buoyancy reverses sign and the particle enters an unsaturated downdraft all the way down to the surface. This strengthens the conclusion drawn from Fig. 2 that particles with higher initial height may actually originate at much lower altitude and have, therefore, a higher MSE than what the initial height could suggest.

One of the messages that emerges from the previous discussion is that precipitation-driven downdrafts tend to have relatively low initial heights, possibly transporting parcels that originated in the bottom kilometer of the troposphere. To provide further evidence to support this statement, we will use three methods, one based on the Lagrangian and two on the Eulerian point of view.

The former one consists of changing the sampling technique we have adopted above, and, instead of considering particles that enter a downdraft and then reach the surface layers inside the core of a cold pool, we simply track all particles in downdrafts, and we follow them until they leave it, regardless of the height where this happens. To be more specific, whenever a particle enters a grid box in which $w \leq -0.5\,\mathrm{m\,s^{-1}}$, its positions are saved for as long as the particle is in a grid box with negative vertical velocity (i.e., $w \leq 0\,\mathrm{m\,s^{-1}}$).

For every particle, we collect the initial height and the final height, which, in contrast to the previous sampling of precipitation-driven downdrafts, does not necessarily have to be in a cold pool or even in the subcloud layer. We also do not allow for a temporal window between the time a particle leaves the downdraft and when its final height is recorded, as done with the other sampling technique. Nevertheless, in the supplemental information we show that considering such a window has no effect on our conclusions.

Next, we define the *height matrix* as the matrix where the (i, j) element contains the density of particles per meter square that entered a downdraft at height z_j and left it at height z_i. Figure 4 shows the logarithm of this matrix. As a guiding rule, numbers in the same column refer to particles that became part of a downdraft at the same height.

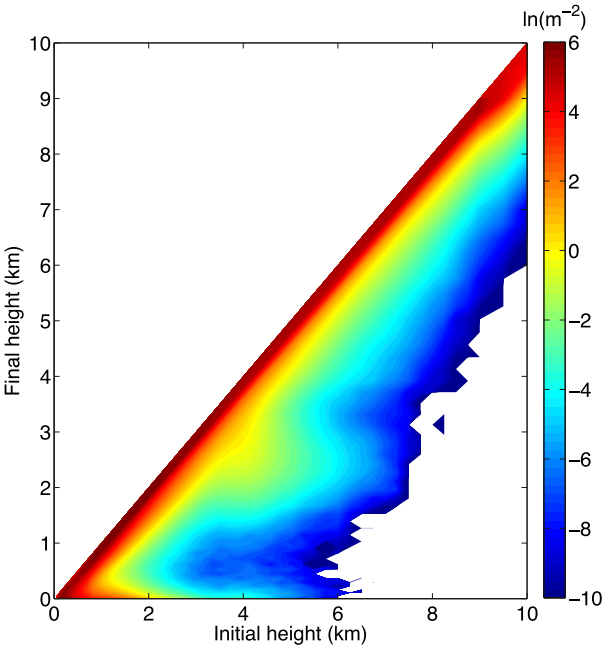

FIG. 4. Logarithm of the height matrix, the (i, j) entry of which indicates the number of particles that became part of a downdraft at height z_j and exited at height z_i.

The figure suggests that, although there are downdrafts at all heights, they do not travel much farther than a few hundred meters. The reason for this, as also suggested by others (see, e.g., Böing et al. 2014), is that, as downdraft parcels descend over large distances, they become dry, and, thus, they start following a dry adiabat. Because the environment above the subcloud layer remains close to a moist adiabat, these parcels quickly lose their negative buoyancy. Furthermore, because precipitating columns are not steady, the negative contributions of rain evaporation and condensate loading to the parcels' buoyancy are also going to become insufficient to maintain the parcels' descent.

One of the most curious features of Fig. 4 that jumps out at the viewer is that downdrafts originating between 3 and 5 km seem to be able to travel a greater distance than those originating at other heights. The average profile of rain evaporation rate shown by the blue curve in Fig. 5, and that of the graupel melting rate shown in green, suggests that particles in downdrafts that cross the levels between 2 and 4 km would experience significant evaporation of rain and melting of graupel, which could provide extra kinetic energy to travel a longer

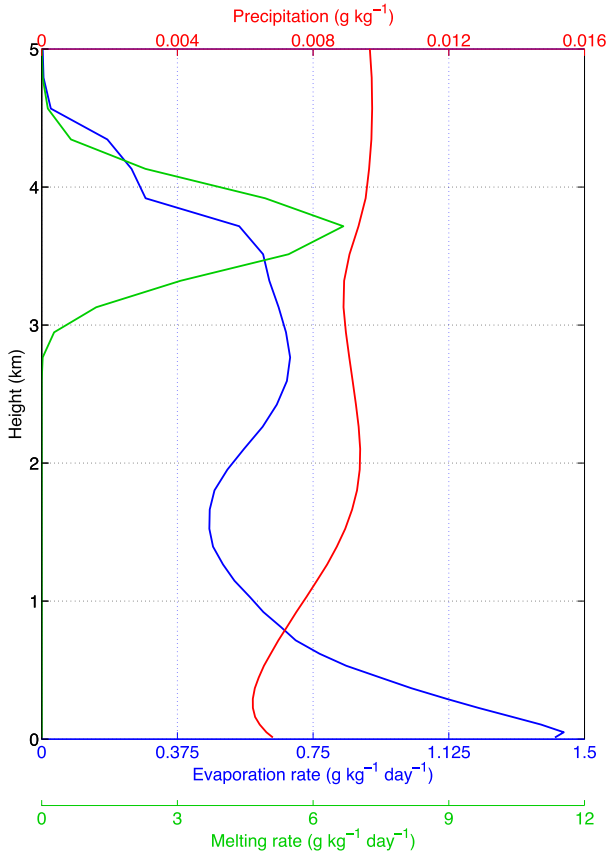

FIG. 5. Time averages of the vertical profiles of rain evaporation rate (blue), graupel melting rate (green), and total precipitating water specific humidity (red) for the bottom 5 km of the model domain.

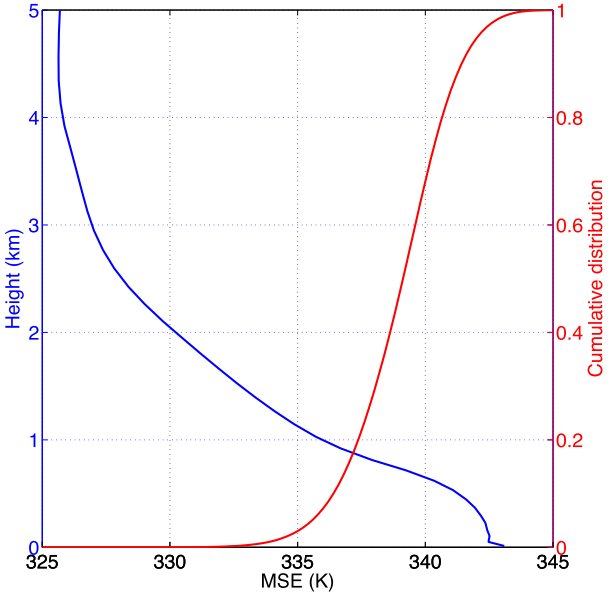

FIG. 6. Time average of the vertical profile of MSE in the environment (blue) and cumulative distribution function of MSE in cold pool cores (red).

distance than particles that descended from much higher or lower altitudes. Notice that, although the peak in melting rate of graupel is almost an order of magnitude higher than the rain evaporation rate at the same altitude, the latent heat of fusion is roughly a factor of 8 smaller than the latent heat of vaporization, so melting of graupel is less efficient in cooling the parcels, and thus in driving the downdraft, than rain evaporation. Finally, we should note that the minimum of evaporation rate between 1 and 2 km is the result of high relative humidity, and thus low saturation deficit, at these altitudes.

The second consistency check that we perform is based on the distribution of MSE in cold pool cores, by which, we remind the reader, we mean those grid cells with a θ_ρ anomaly smaller than -1.5 K. Because adiabatic processes and phase transitions leave MSE roughly unchanged, and because MSE is monotonically decreasing in approximately the bottom 5 km of the troposphere, the presence of low-MSE grid boxes in cold pool cores would be the signature of air parcels originating in the midtroposphere. The red curve in Fig. 6 shows the cumulative distribution function of MSE in cold pool cores during the entire simulation, whereas the blue curve represents the temporal and spatial average of the environmental profile of MSE in the bottom 5 km of the troposphere. The cumulative distribution is concentrated around relatively large values of MSE: the 1st percentile corresponds to an MSE of 333.8 K, which Fig. 6 indicates as the average value in the environment at an altitude of 1.3 km. Notice that MSE is not conserved under mixing, so our estimates are likely to be biased low. Nevertheless, such low altitudes as those indicated above support the claim that air in cold pool cores is unlikely to originate in the midtroposphere.

Finally, the third method that we use to check the consistency of our claim that initial heights of precipitation-driven downdrafts are very low is based on the joint distribution of MSE and vertical velocity at a given height. In particular, Fig. 7 (left) shows the logarithm of the time-averaged joint distribution of MSE anomaly—computed at each time step with respect to the horizontal average—and the vertical velocity at 531 m near the top of the subcloud layer. The black curve highlights the contour corresponding to the value 4.5 of the logarithm of the distribution, which encloses 99.7% of the total number of grid boxes sampled and 87.5% of the total flux of MSE. The contour line shows that most of the MSE flux is given by grid boxes with an MSE anomaly higher than -6 K and relatively small vertical velocities, which suggests that downdrafts from the midtroposphere do not inject much air in the boundary layer.

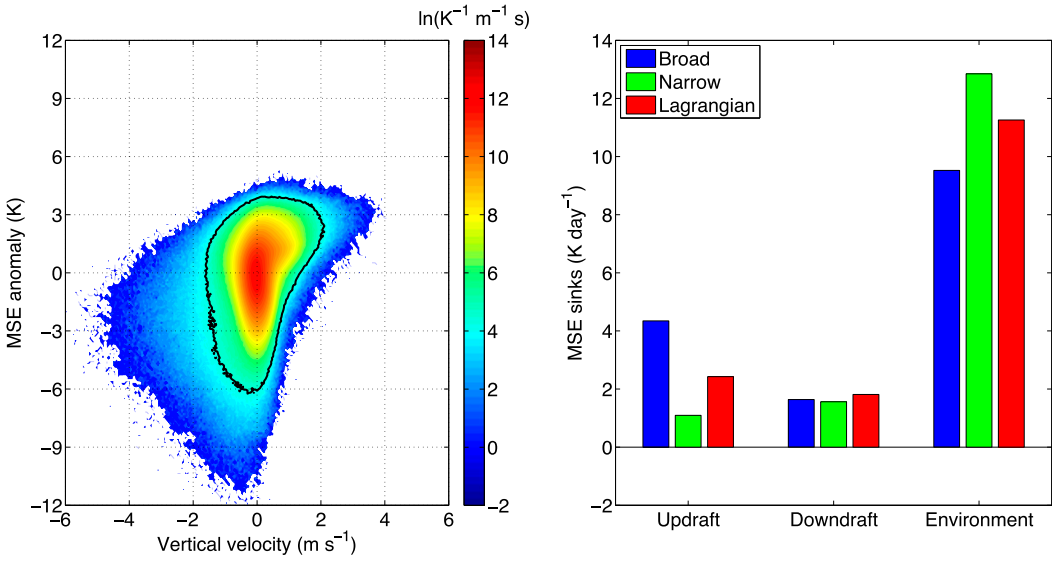

FIG. 7. (left) Logarithm of the joint distribution of vertical velocity and MSE anomaly at 531 m. The black contour corresponds to the isopleth −1 of the logarithmic distribution. (right) Sinks of MSE at the top of the subcloud layer divided by three transport categories: updraft, downdraft, and environment. The blue (green) bars show the rates according to the broad (narrow) definition of the categories introduced in Thayer-Calder and Randall (2015), whereas the red bars show the results obtained using the definition we have given using Lagrangian particles.

b. *On the contribution of precipitation-driven downdrafts to the subcloud-layer MSE*

At this point, it is natural to try and quantify the role of the various transport categories—updrafts, downdrafts, and the environment—in balancing the action of surface fluxes in the subcloud layer. To begin with, let us consider a column of air of unit surface and define the mass contained in the subcloud-layer portion of the column as

$$[\rho] = \int_{z_{\rm sfc}}^{z_{\rm top}} \rho \, dz, \tag{2}$$

where $z_{\rm top}$ and $z_{\rm sfc}$ are the heights of the top of the subcloud layer and the surface. Because mass can be exchanged between the subcloud layer and the free troposphere, if we call M_i the mass flux associated with the i transport category, the temporal variation in mass per unit surface in the subcloud layer can then be written as follows:

$$\frac{\partial [\rho]}{\partial t} = \sum_{i \in T} M_i, \tag{3}$$

where $T = \{\text{updraft, downdraft, environment}\}$. Along the same lines of reasoning, the interaction of the subcloud layer and the free troposphere causes the total MSE per unit surface in the subcloud layer, defined by

$$[\rho h] = \int_{z_{\rm sfc}}^{z_{\rm top}} (\rho h) \, dz, \tag{4}$$

to vary in time according to the following:

$$\frac{\partial [\rho h]}{\partial t} = \sum_{i \in T} M_i h_i, \tag{5}$$

where h_i is the value of MSE at the top of the subcloud layer associated with the transport category i. Notice that the subcloud-layer MSE can also change because of radiative effects, which we will represent as Q_R, and through sensible and latent heat fluxes at the surface, which we will write as SH and LH. It follows that the complete form of Eq. (5) is given by

$$\frac{\partial [\rho h]}{\partial t} = \sum_{i \in T} M_i h_i + (\text{SH} + \text{LH}) + [\rho Q_R], \tag{6}$$

where $[\rho Q_R]$ is defined in a similar fashion to $[\rho h]$. If we now assume that the air in the subcloud layer obeys the Boussinesq approximation and has constant density ρ_0, we can rewrite the left-hand side of the above equation as

$$\frac{\partial [\rho h]}{\partial t} = \int_{z_{\rm sfc}}^{z_{\rm top}} \frac{\partial \rho}{\partial t} h + \rho \frac{\partial h}{\partial t} dz \approx \int_{z_{\rm sfc}}^{z_{\rm top}} \sum_{i \in T} M_i h \, dz + \rho_0 \frac{\partial \overline{h}}{\partial t} Z, \tag{7}$$

where $Z = z_{\text{top}} - z_{\text{sfc}}$ and $\overline{h}$ is the average MSE per unit area in the subcloud layer. This can be further approximated by substituting h in the integral with its value at the top of the subcloud layer h_{top} to give

$$\frac{\partial[\rho h]}{\partial t} \approx Z\left(\sum_{i\in T} M_i h_{\text{top}} + \rho_0 \frac{\partial \overline{h}}{\partial t}\right). \tag{8}$$

Substituting Eq. (8) into Eq. (4), we can write a budget equation for $\overline{h}$:

$$\frac{\partial \overline{h}}{\partial t} = \frac{1}{Z}\sum_{i\in T} w_i(h_i - h_{\text{top}}) + \frac{\text{SH} + \text{LH}}{\rho_0 Z} + \overline{Q_R}, \tag{9}$$

where w_i is the velocity associated with the mass flux M_i and we have substituted the term for the radiative effects with its subcloud-layer average $\overline{Q_R}$. We have derived this formula for an atmospheric column of unit area, but a generalization to an extended domain such as the one we are using is straightforward.

The choice of substituting h with h_{top} in the right side of Eq. (7) may have seemed a bit arbitrary, but it can be fully appreciated in light of Eq. (9), where it is used as a reference to determine the anomalies of MSE at the top of the subcloud layer: both terms h_i and h_{top} are computed at the same height.

Another source of arbitrariness that we have deliberately left vague in our derivation is the definition of the three transport categories. As is well known, the lines between the three categories are blurry enough to allow for multiple ways to address this issue. For example, Thayer-Calder and Randall (2015) used two different definitions to compute the budget of MSE at the top of the boundary layer. In the first one, called *broad*, each grid box at 500-m height is considered a downdraft (updraft) box if it contains any cloud ice, water, or precipitation and has a negative (positive) velocity; if the box does not contain any condensate, it is considered as environment. In the second, called *narrow*, a grid box is considered a downdraft (updraft) box if the vertical velocity is below $-1\,\text{m s}^{-1}$ (above $1\,\text{m s}^{-1}$) for two continuous levels, above and below 500 m, and if it contains any condensate; all other grid boxes are considered environment.

A potential problem with this approach is that some of the properties of a parcel, like its vertical velocity or its liquid water specific humidity, near the top of the boundary layer or cloud base are not necessarily indicative of what transport category the parcel belongs to. For instance, a parcel that will enter a convective updraft might have an LCL at a higher altitude than 500 m, or it might encounter significant convective inhibition, which will then sensibly reduce its vertical velocity, before reaching its LFC. A similar story could also hold true for parcels in downdrafts. We have tried reproducing the results of Thayer-Calder and Randall (2015) at various heights around 500 m and found the conclusions, particularly the contribution by updrafts, to change according to which height is being used.

To remove this ambiguity, we propose a slightly different approach using the Lagrangian particles. Let us go back to the joint distribution of vertical velocity and MSE anomaly shown in Fig. 7 (left). Whenever a particle reaches the top of the subcloud layer, its vertical velocity and the future 60 min of its history are considered. If the particle has positive vertical velocity and, within the specified time frame, acquires positive buoyancy at an altitude higher than 1.5 km, the particle is considered an updraft particle; if the particle has negative vertical velocity and enters a grid box with a density potential temperature anomaly lower than -0.5 K in less than an hour, the particle is considered a downdraft particle. If none of the above conditions are true, the particle is considered an environment particle.

In Fig. 7 (right), we show the contributions to the budget of MSE by the three transport categories. To compare our method with those of Thayer-Calder and Randall (2015), we measure the fluxes of MSE at 531 m, which, in our model, is the height closest to 500 m and also corresponds to the top of the subcloud layer. The blue (green) bars refer to the results obtained using the broad (narrow) definitions explained above, whereas the red bars refer to the method using Lagrangian particles explained above. Like Thayer-Calder and Randall (2015), we find turbulent mixing in the environment to be the biggest contributor to the total MSE sinks, although the contribution from updrafts and downdrafts is not negligible. The export of high MSE air by convective updrafts provides a sink of MSE of $2.43\,\text{K day}^{-1}$, which is 16% of the total, amounting to $15.51\,\text{K day}^{-1}$, whereas the low-MSE air injected in the subcloud layer by precipitation-driven downdrafts reduces MSE at the rate of $1.81\,\text{K day}^{-1}$, 12% of the total. As documented in the supplemental information, we have also tested the sensitivity of the results to the sampling height and found that our conclusions are robust. Of all the heights where we have tested our results, 531 m is the one where the three methods are closest to each other, especially in predicting the contribution by downdrafts. Finally, we want to note that the surface sensible and latent heat fluxes contribute to the budget of MSE with a source equal to $16.28\,\text{K day}^{-1}$, whereas radiative effects provide a sink of $0.86\,\text{K day}^{-1}$.

c. *On the maintenance of precipitation-driven downdrafts*

The next question that we want to focus on in the present work is how to quantify the importance of rain

evaporation and whether it is bigger than that of condensate loading in maintaining precipitation-driven downdrafts. Because we are concerned with the role of rain evaporation from the dynamical point of view, we propose using a purely dynamical quantity such as work to address the problem.

The buoyancy of every particle can be defined in terms of its density potential temperature:

$$b = g\left(\frac{\theta_\rho - \overline{\theta_\rho}}{\overline{\theta_\rho}}\right), \tag{10}$$

where g is the gravitational constant and $\overline{\theta_\rho}$ is the horizontal average of density potential temperature.

At each time step, the contribution to a particle's buoyancy by the condensate loading b_l is given by

$$b_l = -g\left(\frac{q_l\theta}{\overline{\theta_\rho}}\right), \tag{11}$$

from which it follows that the work done by condensate loading on a particle in a precipitation-driven downdraft can be defined as

$$W_l = -g\int_{z_{\text{core}}}^{z_i}\left(\frac{q_l\theta}{\overline{\theta_\rho}}\right)dz, \tag{12}$$

where the integral is taken from the initial height z_i to the height where the particle enters the core of a cold pool z_{core}.

To do the same for rain evaporation, we consider the change in the thermodynamic state of a particle at each time step due to the evaporation of a certain amount of precipitation q_{ev}. Assuming that the evaporation takes place at the end of each time step and that the MSE of a particle is left invariant, the particle's potential temperature will change by

$$\theta_{\text{ev}} = -\frac{L_v}{c_p}q_{\text{ev}}, \tag{13}$$

where L_v is the latent heat of vaporization, equal to 2.5104 MJ kg^{-1} at 0°C, and c_p is the specific heat of dry air at constant pressure, equal to 1004 J kg^{-1} K^{-1}. This change in thermodynamic properties implies a change in the particle's buoyancy that, after a bit of algebra, can be written as follows:

$$b_{\text{ev}} = -\frac{g}{\overline{\theta_\rho}}\left[\frac{L_v}{c_p}(1+\varepsilon q_v - q_l) - \varepsilon\theta\right]q_{\text{ev}}. \tag{14}$$

Much in the same spirit of Eq. (12), we define the work done on a particle by rain evaporation as

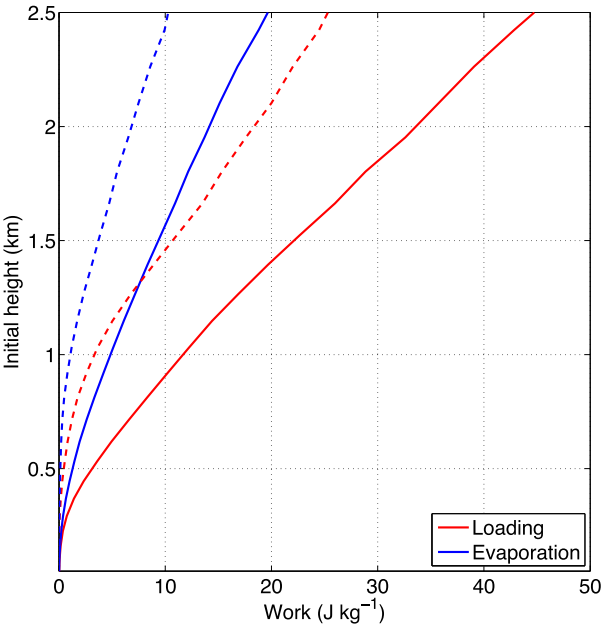

FIG. 8. Comparison between the total work done on Lagrangian particles with different initial heights by different contributions to buoyancy (solid lines) and total buoyancy (dashed lines). Line colors refer to the contributions by condensate loading (red) and the contribution by rain evaporation (blue).

$$W_{\text{ev}} = -g\int_{z_{\text{core}}}^{z_i}\left[\frac{L_v}{c_p}(1+\varepsilon q_v - q_l) - \varepsilon\theta\right]\frac{q_{\text{ev}}}{\overline{\theta_\rho}}\,dz. \tag{15}$$

We will follow the convention that work done on a particle by the environment is positive.

The definition we have given above will provide us with a way to quantify the importance of each mechanism in maintaining a downdraft. Considering again the Lagrangian particles we sampled earlier to construct Fig. 2, we compute the two types of work for each particle and average together the values for particles with the same initial height with the assumption that they have a comparable history and experienced the same phenomena. Figure 8 shows a comparison of the average work done on particles with different initial heights by condensate loading (solid red) and by rain evaporation (solid blue). Notice that, apart from the bottom 300 m, the contribution due to evaporation is smaller than that due to loading by a factor of approximately 0.4.

We can test the consistency of this result by using an Eulerian approach. First, we invoke some approximation to simplify Eqs. (12) and (15). To first order, we can exchange θ_ρ with θ in the denominator, and we can consider q_v and q_l to be much less than 1. Then, since $\varepsilon\theta$ is more than an order of magnitude smaller than the ratio L_v/c_p, we can neglect the second term in square brackets in Eq. (15). With these simplifications, we can write

$$\frac{W_{\rm ev}}{W_l} \approx \left(\frac{L_{v_0}}{c_p \Theta}\right) \frac{\int q_{\rm ev}\, dz}{\int q_l\, dz}, \tag{16}$$

where L_v has been approximated by its value at 0°C, 2.5104 MJ kg^{-1}, and Θ represents a scale for the potential temperature and equals 300 K. To evaluate the integrals in the above equation, we will consider a parcel descending from an altitude of 1 km, the location of the peak in Fig. 2. For every height, we compute the distribution of negative vertical velocities of grid boxes where q_p is nonzero, and we assume that the vertical velocity of the parcel we are considering equals the median of the distribution. This construction is to ensure that the parcel is representative of parcels within precipitation-driven downdrafts.

The integral in the denominator is proportional to the average value of liquid water content of the parcel, and it can be quickly put in discrete form as

$$\int_{z_{\rm sfc}}^{z_i} q_l\, dz = \sum_{i=k_{\rm sfc}}^{k_i} (q_l)_i \Delta z_i, \tag{17}$$

where Δz_i is the vertical grid spacing at height z_i, and $k_{\rm sfc}$ and k_i are the model levels corresponding to heights $z_{\rm sfc}$ and z_i, respectively.

The integral in the numerator requires a little more care. The integrand represents the specific humidity of liquid water that is evaporated into the parcel as it travels a distance equal to dz. By definition, this can be rewritten as

$$q_{\rm ev} = (\delta q_v^{\rm src})\, dt = (\delta q_v^{\rm src}) \frac{dz}{w}, \tag{18}$$

where $(\delta q_v^{\rm src})$ is the rate of generation of water vapor by rain evaporation and dt is the time it takes the parcel to go from $z + dz$ to z. It follows that we can evaluate the integral in the numerator of Eq. (16) by computing the sum:

$$\int_{z_{\rm sfc}}^{z_i} q_{\rm ev}\, dz = \sum_{i=k_{\rm sfc}}^{k_i} (\delta q_v^{\rm src})_i \left(\frac{\Delta z_i^2}{w_i}\right). \tag{19}$$

The liquid water specific humidity and the evaporation rate can be diagnosed from the model outputs, and their values in the bottom 5 km can be seen in Fig. 5. Plugging in all the numbers, we can compute that the ratio between the work done by rain evaporation and that done by condensate loading is 0.36, which compares reasonably well with the estimate of 0.41 that is obtained using the Lagrangian particles.

As discussed by Davies-Jones (2003), buoyancy in a nonhomogeneous environment, such as the one we are examining, is an ill-defined concept. Instead, what should really be considered as the effective buoyancy experienced by a parcel is the sum of the Archimedean buoyancy, which we have defined in Eq. (1), and the buoyancy-related pressure gradient, which cannot be determined locally. Recently, it has been shown (Torri et al. 2015; Jeevanjee and Romps 2015) that parcels that have been triggered by cold pools and that are ascending toward their LFC are subject to a significant cancellation between buoyancy and buoyancy-related pressure gradients. This leads us to ask whether our conclusions on the minor role played by rain evaporation in maintaining the downdraft are robust when buoyancy-related pressure gradients are taken into account. To address this point, for simplicity, we first assume that the contributions to the buoyancy-related pressure gradients at every moment can be viewed as approximately proportional to the contributions to the Archimedean buoyancy by a factor given by the ratio of the buoyancy-related pressure gradient and buoyancy, which we will refer to as *buoyancy ratio* β:

$$\beta \stackrel{\rm def}{=} \frac{\partial_z p_b}{b} \approx \frac{\partial_z p_{b,l}}{b_l} \approx \frac{\partial_z p_{b,\rm ev}}{b_{\rm ev}}, \tag{20}$$

where p_b is the buoyancy-related pressure perturbation and $p_{b,l}$ and $p_{b,\rm ev}$ are its contributions due to condensate loading and rain evaporation, respectively.

In this way, we can reconstruct the various contributions to the buoyancy-related pressure gradients very simply, and the calculation of the work done by these contributions is straightforward.

The two contributions to the work done by total buoyancy—by which we mean the sum of the Archimedean buoyancy and the buoyancy-related pressure gradients (Torri et al. 2015)—are shown by the dashed lines in Fig. 8, and they suggest that our conclusions are robust, even when buoyancy-related pressure gradients are taken into account. A close inspection of the vertical profiles of buoyancy ratio (not shown) suggests that this quantity tends to be maximum in magnitude in the subcloud layer, with values approaching −1, and becomes closer to 0 with increasing height. This explains why the particles that seem most affected by the correction are those with an initial height smaller than 1 km.

A natural question that arises now is whether condensate loading dominates over rain evaporation at any moment during the particle's descent in the downdraft or if the two mechanisms are important at different stages. To investigate this, instead of considering an integrated quantity such as the work, we look directly at

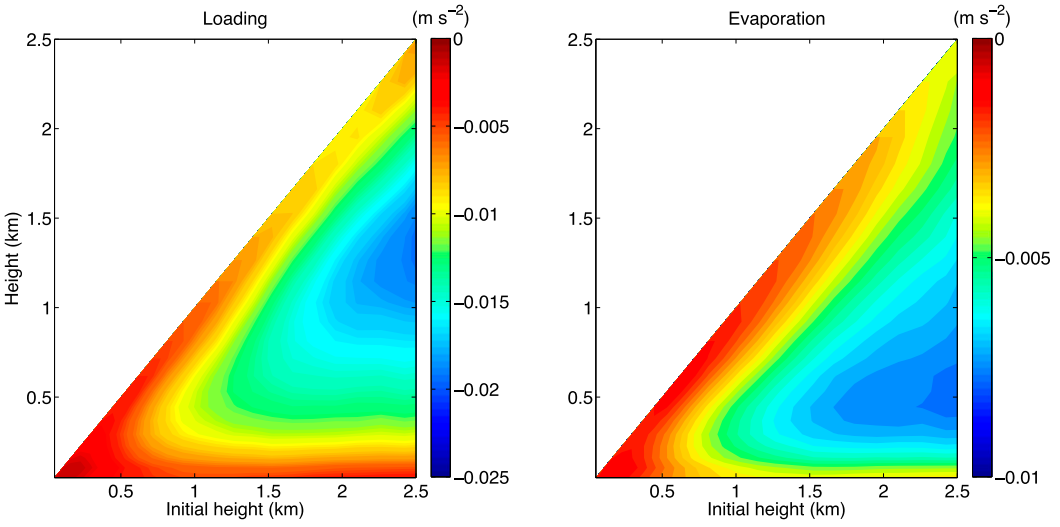

FIG. 9. Vertical profiles of the time-averaged change of buoyancy due to (left) condensate loading and (right) rain evaporation for Lagrangian particles in precipitation-driven downdrafts with different initial heights.

the contributions to buoyancy given by the two mechanisms. We present the results in Fig. 9, with Fig. 9 (left) referring to the contribution from condensate loading and Fig. 9 (right) referring to that from rain evaporation.

As for the construction of Fig. 8, we use the initial height of a particle as a sampling criterion: the histories of particles with the same initial height are averaged together, and the results are presented for each value of initial height. Thus, each column in Fig. 9 represents the vertical profile of the average contribution to the buoyancy of particles having an initial height given by the abscissa of the column in the figure.

In comparing the two plots, one should be careful to notice that the color bars differ by a factor of 2.5. This was done to make it possible for the eye to easily distinguish the main features of each contribution at every height for different types of particles. Therefore, in spite of the immediate appearance, condensate loading contributes to buoyancy more than evaporation almost everywhere, except for very near the surface, where both contributions seem of equal magnitude.

Another interesting feature of the two plots is that, for any initial height, the altitude where each contribution is maximum is different: for loading, the peak tends to be in the initial stages of the downdraft, whereas for evaporation the maximum is in the subcloud layer.

For the condensate loading, the peak is essentially due to two factors: the first is that rain columns are not steady but, rather, quickly grow to a maximum and then decay over time; the second is the fact that precipitating water in a rain column flows through the Lagrangian particles or, in other words, the vertical velocity of the particles is typically smaller than the terminal velocity of raindrops.

To check that the latter is true, we can consider Fig. 10, which shows the average vertical velocity experienced by particles of various initial heights at different stages of their descent. Above the bottom few hundred meters, where the hydrostatic pressure perturbation in the core of cold pools causes the downdraft to slow down, the vertical velocities experienced by the descending particles are roughly between −0.5

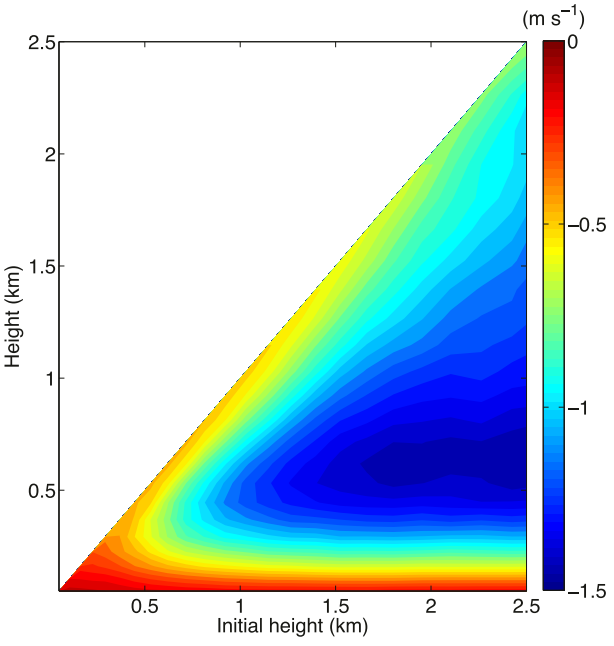

FIG. 10. Vertical profiles of time-averaged vertical velocities for Lagrangian particles in precipitation-driven downdrafts with different initial heights.

and $-1.5\,\mathrm{m\,s^{-1}}$. Considering the precipitation rate and the precipitating liquid water content in the grid boxes of the bottom 3 km of the model, we can estimate that the average terminal velocities of raindrops are between -5 and $-6\,\mathrm{m\,s^{-1}}$, well outside the range of average velocities of Lagrangian particles within precipitation-driven downdrafts. As a side note, we want to point out that the terminal velocities diagnosed from the model are consistent with data from observations: the terminal velocities for raindrops with diameters between 1 and 5 mm go from -4.03 to $-9.09\,\mathrm{m\,s^{-1}}$ (Gunn and Kinzer 1949).

To understand why the contribution to buoyancy by rain evaporation—and, more generally, the evaporation rate—peaks at low altitudes, we must take a step back and think about how liquid water evaporates in a particle in the downdraft. It is well known (see, e.g., Kamburova and Ludlam 1966; Betts and Silva Dias 1979) that evaporation of a falling raindrop of radius r and mass m can be modeled as a diffusion process:

$$\frac{Dm}{Dt} = 4\pi D C_v \rho r (q_v - q_{\mathrm{sat}}), \tag{21}$$

where D is the diffusion coefficient of water vapor in air, C_v is a ventilation factor, ρ is the density of the parcel, and q_{sat} is the saturation specific humidity. If we consider an air parcel with volume V and assume, for simplicity, that it contains N raindrops of equal radius R, then the liquid water content of the parcel can be simply related to the radius of the raindrop by the following:

$$q_l = \left(\frac{4\pi\rho_l N}{3\rho V}\right) R^3 \overset{\mathrm{def}}{=} \left(\frac{4\pi D C_v}{VK}\right)^3 R^3, \tag{22}$$

where ρ_l is the density of liquid water, and, for simplicity, we have defined a new variable K as

$$K = D C_v \left(\frac{48\pi^2\rho}{N V^2 \rho_l}\right)^{1/3}. \tag{23}$$

With some simple algebra, it is easy to show that Eq. (21) can be rewritten as

$$\frac{Dq_l}{Dt} = K q_l^{1/3} (q_v - q_{\mathrm{sat}}). \tag{24}$$

Figure 11 shows the average product of the cubic root of the cloud liquid water and the saturation deficit for particles with different initial heights. Assuming that K is constant at all heights and for particles from all initial heights, the figure can be compared directly with the contribution to buoyancy by rain evaporation. Notice that, for each initial height, the profiles show a peak in the subcloud layer, roughly at the same height where the contribution by evaporation is maximum. Thus, one could say that the peak in evaporation rate in the subcloud layer is the result of two factors: the saturation deficit, which increases as the surface is approached (not shown), and the liquid water content of each parcel, which, as can be inferred from Fig. 9 (left), decreases in the latter stages of the downdraft.

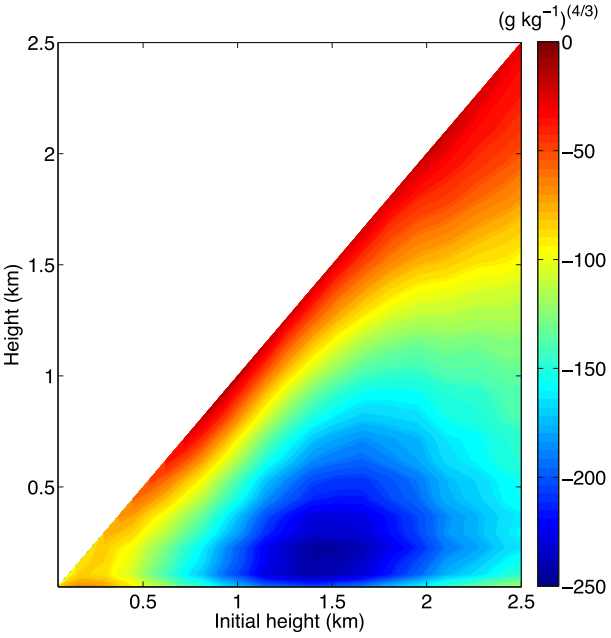

FIG. 11. Profiles of the time average of the cubic root of liquid water specific humidity multiplied by the saturation deficit for Lagrangian particles in precipitation-driven downdrafts.

Given the crude assumptions that we have made to derive Eq. (24), it is not surprising that the agreement between Fig. 11 and Fig. 9 (right) is only partial: unlike the profiles of the contribution by evaporation, the magnitude of the product seems generally to decrease for particles with increasing initial height. We expect that accounting for a distribution of radii and by allowing the number of raindrops N to vary with height and initial height would improve the agreement. However, we want to stress that this mismatch does not change our conclusions.

4. Conclusions

We have used an LPDM to address two important aspects regarding the dynamics of precipitation-driven downdrafts: namely, their initial height and the role played by rain evaporation in maintaining them. By sampling all the Lagrangian particles that are injected in the coldest regions of cold pools in the subcloud layer by downdrafts, we have determined that the vast majority of such particles start descending from a height lower

than 2.5 km in the model domain. Looking at the position of the particles at times prior to their entrance in a precipitation-driven downdraft, we have shown that most of them originate in the subcloud layer; almost none come from high altitudes.

As a further check, we have broadened our sampling criterion and considered all particles that are part of downdrafts at any height, regardless of whether they will be injected in a cold pool or not. With this, we have shown that downdrafts exist at all heights in the model but a few hundred meters past their initial height. This provided additional support to the claim that precipitation-driven downdrafts originate at very low altitudes and do not, therefore, bring very cold and dry air into the subcloud layer.

This led us to the question of what balances the surface fluxes and keeps the boundary layer MSE relatively steady in time. Using a definition of the three transport categories—updraft, downdraft, and environment—based on the Lagrangian particles, we have concluded that most of the MSE sink is to be attributed to turbulent mixing or wave activity in the environment, although the contributions by updrafts and downdrafts are non-negligible, their sum accounting for 28% of the total.

We then proceeded to quantify the role of rain evaporation in maintaining the precipitation-driven downdrafts. By looking at the total work done on each Lagrangian particle that is injected in the core of a cold pool by a downdraft and distinguishing the contribution due to condensate loading from that due to rain evaporation, we showed that the latter is smaller than the former, roughly by a factor of 0.4.

Considering the change of the Lagrangian particles' buoyancy due to condensate loading and rain evaporation, we showed that the former is bigger than the latter at all heights and tends to be maximum in the first part of the downdraft descent; on the other hand, the latter is highest in the second part of the descent, when the particles are in the subcloud layer.

We interpreted the first effect as due to the fact that the terminal velocity of rain droplets is higher in magnitude than the vertical velocity of the descending Lagrangian particles and that the liquid water content associated with each rain shaft is not constant in time.

As for rain evaporation, we have argued that its maximum in the subcloud layer is simply the combination of saturation deficit and the liquid water specific humidity, which enters the equation for evaporation rates only in a cubic root. In particular, even though the precipitation experienced by Lagrangian particles is largest in the initial stages of the downdraft, the small saturation deficit does not allow for large amounts of rain to be evaporated. Only in the subcloud layer is the saturation deficit large enough to make the contribution of rain evaporation in maintaining the downdraft more significant.

Since the dynamics of downdraft maintenance is tightly related to microphysical processes such as rain evaporation, it seems natural to ask how sensitive our conclusions are to the microphysics scheme. For this reason, we have run the same simulation described in section 2 using the two-moment microphysics scheme introduced in Morrison et al. (2005) and have carried out the same analysis described in the previous section. Apart from some slight differences, we found that the conclusions of this study are robust.

Although this robustness gives us some confidence over the generality of our findings, we want to stress that we have only considered an oceanic case in RCE with no wind shear and, a priori, we do not expect our results to hold for other cases. For instance, it is very well possible that, in a continental case with a much drier boundary layer, evaporation of rain will play a much bigger role in maintaining the downdraft. This could also be the case in the presence of wind: a considerable vertical wind shear might change the geometry of a precipitating cloud, exposing a larger part of a precipitating column to an unsaturated environment.

Finally, the conceptual framework that emerges from this manuscript can have important consequences for climate models. In particular, our findings suggest that the premises on which the BLQE hypothesis is founded—that downdrafts are responsible for most of the MSE sink in the boundary layer—may not be realized in nature. Although some models have been shown to better reproduce certain features of the tropical climate, such as the MJO, when strong convective downdrafts are included (Mishra and Sahany 2011), we suggest that the key for a more accurate simulation of the tropical atmosphere is in improving parameterizations of the transport due to turbulent mixing or wave activity in the environment. Mesoscale organization of convective systems, absent in this study, may also affect the results. Notwithstanding these additional scenarios, which clearly warrant further investigations, our analysis of the oceanic RCE case addresses a basic scenario that is potentially representative of large areas over the tropical oceans with modest wind shears.

Although they play only a secondary role in the MSE budget of the tropical boundary layer, downdrafts still remain an important component of convective systems that should be included in convective parameterizations. Our results could also be useful for this task: first, they indicate the initial height tends to be in the lower troposphere; second, the fact that rain evaporation contributes much less than condensate loading in maintaining the downdraft indicates that downdrafts might be more

sensitive to the model precipitation rate rather than to the relative humidity.

Acknowledgments. The authors thank Marat Khairoutdinov for access to the SAM code and Paul Edmon for precious and tireless assistance with the Harvard Odyssey cluster on which the simulations were run. This research was partially supported by the Office of Biological and Environmental Research of the U.S. Department of Energy under Grant DE-SC0008679 as part of the ASR program and by NSF Grants AGS-1062016 and AGS-1260380.

REFERENCES

Arakawa, A., and W. H. Schubert, 1974: Interaction of a cumulus cloud ensemble with the large-scale environment, Part I. *J. Atmos. Sci.*, **31**, 674–701, doi:10.1175/1520-0469(1974)031<0674:IOACCE>2.0.CO;2.

Barnes, G. M., and M. Garstang, 1982: Subcloud layer energetics of precipitating convection. *Mon. Wea. Rev.*, **110**, 102–117, doi:10.1175/1520-0493(1982)110<0102:SLEOPC>2.0.CO;2.

Betts, A. K., 1976: The thermodynamic transformation of the tropical subcloud layer by precipitation and downdrafts. *J. Atmos. Sci.*, **33**, 1008–1020, doi:10.1175/1520-0469(1976)033<1008:TTTOTT>2.0.CO;2.

——, and M. F. Silva Dias, 1979: Unsaturated downdraft thermodynamics in cumulonimbus. *J. Atmos. Sci.*, **36**, 1061–1071, doi:10.1175/1520-0469(1979)036<1061:UDTIC>2.0.CO;2.

Böing, S. J., H. J. J. Jonker, W. A. Nawara, and A. P. Siebesma, 2014: On the deceiving aspects of mixing diagrams of deep cumulus convection. *J. Atmos. Sci.*, **71**, 56–68, doi:10.1175/JAS-D-13-0127.1.

Braham, R. R., Jr., 1952: The water and energy budgets of the thunderstorm and their relation to thunderstorm development. *J. Atmos. Sci.*, **9**, 227–242, doi:10.1175/1520-0469(1952)009<0227:TWAEBO>2.0.CO;2.

Byers, H. R., and R. R. Braham, 1949: The thunderstorm. U. S. Weather Bureau Tech. Rep., 287 pp. [NTIS PB-234515.]

Cotton, W. R., G. Bryan, and S. C. van den Heever, 2011: Cumulonimbus clouds and severe convective storms. *Storm and Cloud Dynamics—The Dynamics of Clouds and Precipitating Mesoscale Systems*, G. B. William Cotton and S. van den Heever, Eds., International Geophysics Series, Vol. 99, Academic Press, 315–454, doi:10.1016/S0074-6142(10)09914-6.

Davies-Jones, R., 2003: An expression for effective buoyancy in surroundings with horizontal density gradients. *J. Atmos. Sci.*, **60**, 2922–2925, doi:10.1175/1520-0469(2003)060<2922:AEFEBI>2.0.CO;2.

Emanuel, K. A., 1989: The finite-amplitude nature of tropical cyclogenesis. *J. Atmos. Sci.*, **46**, 3431–3456, doi:10.1175/1520-0469(1989)046<3431:TFANOT>2.0.CO;2.

——, 1994: *Atmospheric Convection*. Oxford University Press, 592 pp.

Fankhauser, J. C., 1976: Structure of an evolving hailstorm, Part II: Thermodynamic structure and airflow in the near environment. *Mon. Wea. Rev.*, **104**, 576–587, doi:10.1175/1520-0493(1976)104<0576:SOAEHP>2.0.CO;2.

Fujita, T. T., 1985: The downburst: Microburst and macroburst. Satellite and Mesometeorology Research Paper 210, 122 pp.

——, 1986: DFW microburst on August 2, 1985. Satellite and Mesometeorology Research Paper 217, 155 pp.

Gunn, R., and G. D. Kinzer, 1949: The terminal velocity of fall for water droplets in stagnant air. *J. Meteor.*, **6**, 243–248, doi:10.1175/1520-0469(1949)006<0243:TTVOFF>2.0.CO;2.

Humphreys, W. J., 1914: The thunderstorm and its phenomena. *Mon. Wea. Rev.*, **42**, 348–380, doi:10.1175/1520-0493(1914)42<348:TTAIP>2.0.CO;2.

Jeevanjee, N., and D. M. Romps, 2015: Effective buoyancy, inertial pressure, and the mechanical generation of boundary layer mass flux by cold pools. *J. Atmos. Sci.*, **72**, 3199–3213, doi:10.1175/JAS-D-14-0349.1.

Johnson, R. H., and M. E. Nicholls, 1983: A composite analysis of the boundary layer accompanying a tropical squall line. *Mon. Wea. Rev.*, **111**, 308–319, doi:10.1175/1520-0493(1983)111<0308:ACAOTB>2.0.CO;2.

Kamburova, P. L., and F. H. Ludlam, 1966: Rainfall evaporation in thunderstorm downdraughts. *Quart. J. Roy. Meteor. Soc.*, **92**, 510–518, doi:10.1002/qj.49709239407.

Khairoutdinov, M. F., and D. A. Randall, 2003: Cloud resolving modeling of the ARM summer 1997 IOP: Model formulation, results, uncertainties, and sensitivities. *J. Atmos. Sci.*, **60**, 607–625, doi:10.1175/1520-0469(2003)060<0607:CRMOTA>2.0.CO;2.

Kingsmill, D. E., and R. A. Houze, 1999: Thermodynamic characteristics of air flowing into and out of precipitating convection over the west Pacific warm pool. *Quart. J. Roy. Meteor. Soc.*, **125**, 1209–1229, doi:10.1002/qj.1999.49712555606.

Knupp, K. R., 1987: Downdrafts within High Plains cumulonimbi. Part I: General kinematic structure. *J. Atmos. Sci.*, **44**, 987–1008, doi:10.1175/1520-0469(1987)044<0987:DWHPCP>2.0.CO;2.

——, 1988: Downdrafts within High Plains cumulonimbi. Part II: Dynamics and thermodynamics. *J. Atmos. Sci.*, **45**, 3965–3982, doi:10.1175/1520-0469(1988)045<3965:DWHPCP>2.0.CO;2.

——, and W. R. Cotton, 1985: Convective cloud downdraft structure: An interpretive survey. *Rev. Geophys.*, **23**, 183–215, doi:10.1029/RG023i002p00183.

Lemon, L. R., 1976: The flanking line, a severe thunderstorm intensification source. *J. Atmos. Sci.*, **33**, 686–694, doi:10.1175/1520-0469(1976)033<0686:TFLAST>2.0.CO;2.

Lin, Y.-L., R. D. Farley, and H. D. Orville, 1983: Bulk parameterization of the snow field in a cloud model. *J. Climate Appl. Meteor.*, **22**, 1065–1092, doi:10.1175/1520-0450(1983)022<1065:BPOTSF>2.0.CO;2.

Mal, S., and B. N. Desai, 1938: The mechanism of thundery conditions at Karachi. *Quart. J. Roy. Meteor. Soc.*, **64**, 525–537, doi:10.1002/qj.49706427618.

Miller, M. J., and A. K. Betts, 1977: Traveling convective storms over Venezuela. *Mon. Wea. Rev.*, **105**, 833–848, doi:10.1175/1520-0493(1977)105<0833:TCSOV>2.0.CO;2.

Mishra, S. K., and S. Sahany, 2011: Sensitivity of Kelvin waves and Madden–Julian oscillation to convective downdrafts in the NCAR-CAM3. *Atmos. Sci. Lett.*, **12**, 281–287, doi:10.1002/asl.334.

Morrison, H., J. A. Curry, and V. I. Khvorostyanov, 2005: A new double-moment microphysics parameterization for application in cloud and climate models. Part I: Description. *J. Atmos. Sci.*, **62**, 1665–1677, doi:10.1175/JAS3446.1.

Newton, C. W., 1950: Structure and mechanism of the prefrontal squall line. *J. Atmos. Sci.*, **7**, 210–222, doi:10.1175/1520-0469(1950)007<0210:SAMOTP>2.0.CO;2.

Nie, J., and Z. Kuang, 2012: Responses of shallow cumulus convection to large-scale temperature and moisture perturbations: A comparison of large-eddy simulations and a convective parameterization based on stochastically entraining parcels. *J. Atmos. Sci.*, **69**, 1936–1956, doi:10.1175/JAS-D-11-0279.1.

Normand, C., 1946: Energy in the atmosphere. *Quart. J. Roy. Meteor. Soc.*, **72**, 145–167, doi:10.1002/qj.49707231202.

Proctor, F. H., 1988: Numerical simulations of an isolated microburst. Part I: Dynamics and structure. *J. Atmos. Sci.*, **45**, 3137–3160, doi:10.1175/1520-0469(1988)045<3137:NSOAIM>2.0.CO;2.

——, 1989: Numerical simulations of an isolated microburst. Part II: Sensitivity experiments. *J. Atmos. Sci.*, **46**, 2143–2165, doi:10.1175/1520-0469(1989)046<2143:NSOAIM>2.0.CO;2.

Purdom, J. F. W., 1976: Some uses of high-resolution GOES imagery in the mesoscale forecasting of convection and its behavior. *Mon. Wea. Rev.*, **104**, 1474–1483, doi:10.1175/1520-0493(1976)104<1474:SUOHRG>2.0.CO;2.

Raymond, D. J., 1994: Convective processes and tropical atmospheric circulations. *Quart. J. Roy. Meteor. Soc.*, **120**, 1431–1455, doi:10.1002/qj.49712052002.

——, 1995: Regulation of moist convection over the west Pacific warm pool. *J. Atmos. Sci.*, **52**, 3945–3959, doi:10.1175/1520-0469(1995)052<3945:ROMCOT>2.0.CO;2.

Rotunno, R., and J. Klemp, 1985: On the rotation and propagation of simulated supercell thunderstorms. *J. Atmos. Sci.*, **42**, 271–292, doi:10.1175/1520-0469(1985)042<0271:OTRAPO>2.0.CO;2.

——, J. B. Klemp, and M. L. Weisman, 1988: A theory for strong, long-lived squall lines. *J. Atmos. Sci.*, **45**, 463–485, doi:10.1175/1520-0469(1988)045<0463:ATFSLL>2.0.CO;2.

Thayer-Calder, K., and D. Randall, 2015: A numerical investigation of boundary layer quasi-equilibrium. *Geophys. Res. Lett.*, **42**, 550–556, doi:10.1002/2014GL062649.

Tompkins, A. M., 2001: Organization of tropical convection in low vertical wind shears: The role of water vapor. *J. Atmos. Sci.*, **58**, 529–545, doi:10.1175/1520-0469(2001)058<0529:OOTCIL>2.0.CO;2.

Torri, G., Z. Kuang, and Y. Tian, 2015: Mechanisms for convection triggering by cold pools. *Geophys. Res. Lett.*, **42**, 1943–1950, doi:10.1002/2015GL063227.

Wakimoto, R. M., C. J. Kessinger, and D. E. Kingsmill, 1994: Kinematic, thermodynamic, and visual structure of low-reflectivity microbursts. *Mon. Wea. Rev.*, **122**, 72–92, doi:10.1175/1520-0493(1994)122<0072:KTAVSO>2.0.CO;2.

Weaver, J. F., and S. P. Nelson, 1982: Multiscale aspects of thunderstorm gust fronts and their effects on subsequent storm development. *Mon. Wea. Rev.*, **110**, 707–718, doi:10.1175/1520-0493(1982)110<0707:MAOTGF>2.0.CO;2.

Weisman, M. L., and R. Rotunno, 2004: ''A theory for strong long-lived squall lines'' revisited. *J. Atmos. Sci.*, **61**, 361–382, doi:10.1175/1520-0469(2004)061<0361:ATFSLS>2.0.CO;2.

——, J. B. Klemp, and R. Rotunno, 1988: Structure and evolution of numerically simulated squall lines. *J. Atmos. Sci.*, **45**, 1990–2013, doi:10.1175/1520-0469(1988)045<1990:SAEONS>2.0.CO;2.

Zipser, E. J., 1969: The role of organized unsaturated convective downdrafts in the structure and rapid decay of an equatorial disturbance. *J. Appl. Meteor.*, **8**, 799–814, doi:10.1175/1520-0450(1969)008<0799:TROOUC>2.0.CO;2.